

## 7 Simulating radiation effects and signal response in silicon sensors

*Editors:* M. Bomben<sup>a</sup>, J. Sonneveld<sup>b</sup>.

*Contributing authors:* M. Benoit<sup>c</sup>, M. Bomben<sup>a</sup>, E. Chabert<sup>d</sup>, T. Lari<sup>e</sup>, J. Llorente Merino<sup>f</sup>, B. Nachman<sup>g</sup>, L. Rossini<sup>h</sup>, P. Sabatini<sup>i</sup>, J. Sonneveld<sup>b</sup>, C. Suarez<sup>j</sup>, M. Swartz<sup>j</sup>, T. Szumlak<sup>k</sup>, A. Wang<sup>l</sup>.

<sup>a</sup>LPNHE & University of Paris, France

<sup>b</sup>Nikhef, Amsterdam, Netherlands

<sup>c</sup>Brookhaven National Laboratory (BNL), New York, USA

<sup>d</sup>Hubert Curien Pluridisciplinary Institute (IPHC), Strasbourg, France

<sup>e</sup>INFN, Milan, Italy

<sup>f</sup>Simon Fraser University, Burnaby, Canada

<sup>g</sup>Lawrence Berkeley National Laboratory, USA

<sup>h</sup>University of Milan and INFN, Milan, Italy<sup>7</sup>

<sup>i</sup>Institute for Corpuscular Physics (IFIC), Centro Mixto Universidad de Valencia - CSIC

<sup>j</sup>Johns Hopkins University, Baltimore, USA

<sup>k</sup>AGH University of Science and Technology, Krakow, Poland

<sup>l</sup>University of Wisconsin-Madison, USA

Simulating the effects of radiation on signal response in silicon sensors is crucial for accurately predicting detector performance throughout the lifetime of the experiment. This, in turn, improves the reconstruction accuracy of proton–proton collisions and helps maintain the experiment’s physics reach. In what follows, the strategies implemented by the LHC experiments to correctly simulate the evolution of silicon tracking performance with luminosity will be presented.

As already discussed in Section 2, the main macroscopic effects on silicon tracking devices resulting from radiation damage are: increase of leakage current, change of operational voltage, and signal loss. They are the result of phenomena happening at a microscopic level which are a consequence of the creation of defects that act as deep levels in the semiconductor energy gap. These levels can trap charged carriers – reducing the signal and modifying the electric field distribution inside the sensors. They also act as additional generation levels and these dynamics give rise to the aforementioned change in performance at a macroscopic level. These effects are further complicated by the temperature history, since the thermal motion in the silicon lattice leads to annealing phenomena that cause new defects to be formed or existing defects to dissociate.

The general parameterization of radiation damage simulation for silicon tracking detectors of LHC experiments should model the change of the electric field distribution in the silicon bulk and the signal loss with the accumulated luminosity. These two effects in turn also have an impact on other observables such as spatial resolution through modification of cluster sizes and Lorentz angle deflection.

Before presenting the details and results of the different LHC experiments, some general aspects of sensor simulations are discussed. Particles originating from collisions in the LHC deposit charge in silicon detectors by ionizing the silicon bulk: the deposited charge drifts through the sensor to an electrode, then the analogue signal is digitized, buffered and read out.

In general, for the LHC experiments the following are important to consider in simulation.

**Electric field:** as a result of radiation damage, the shape of the electric field inside the bulk of the sensor

This chapter should be cited as: Simulating radiation effects in silicon sensors and modelling charge response, Eds. M. Bomben, J. Sonneveld, DOI: [10.23731/CYRM-2021-001.123](https://doi.org/10.23731/CYRM-2021-001.123), in: Radiation effects in the LHC experiments: Impact on detector performance and operation, Ed. Ian Dawson,

CERN Yellow Reports: Monographs, CERN-2021-001, DOI: [10.23731/CYRM-2021-001](https://doi.org/10.23731/CYRM-2021-001), p. 123.

© CERN, 2021. Published by CERN under the [Creative Commons Attribution 4.0 license](https://creativecommons.org/licenses/by/4.0/).

<sup>7</sup>Now at DESY, Hamburg and Zeuthen, Germany

changes with fluence. Simulations of the three-dimensional profile of the electric field can be obtained with software based on technology computer-aided design (TCAD). Inputs for the electric field simulation are the sensor type, doping, and geometry, the irradiation fluence, the bias voltage, and the temperature.

**Lorentz angle:** the Lorentz angle  $\theta_L$  is the deflection angle for carriers in presence of an electric field  $\vec{E}$  and a magnetic field  $\vec{B}$ ; and is defined as the angle between the drift direction and the electric field. For a carrier travelling from an initial bulk depth  $z_i$ <sup>8</sup> to a final depth  $z_f$  inside the bulk of the sensor, the Lorentz angle  $\theta_L$  can be expressed by:

$$\tan \theta_L(z_i, z_f) = \frac{rB}{|z_f - z_i|} \int_{z_i}^{z_f} \mu(E(z)) dz, \quad (33)$$

where  $\mu$  is the charged carrier mobility,  $r$  is the Hall scattering factor,  $B$  is the magnetic field magnitude, and  $E(z)$  is the electric field as a function of the position. It is then possible to note that a change in electric field resulting from radiation damage will also impact the Lorentz angle, since the mobility depends on the electric field.

**Ramo potential and induced charge:** moving charges inside the bulk induce a signal onto the collecting electrodes. The induced signal can be calculated using the Shockley–Ramo theorem [1,2]. The induced signal by a charge  $q$  moving from the initial position  $\vec{x}_i$  to the final position  $\vec{x}_f$  is:

$$Q_{\text{induced}} = -q[\phi_w(\vec{x}_f) - \phi_w(\vec{x}_i)], \quad (34)$$

where  $\phi_w$  is the Ramo potential. The Ramo potential depends only on the geometry of the electrodes and the bulk thickness, and therefore it is evaluated once per geometry. The Ramo potential can be evaluated using TCAD tools replacing silicon with vacuum in the simulated structure so only electrodes are left.

**Charge trapping:** the charge carriers can be trapped by radiation-induced deep defects<sup>9</sup>, with a characteristic trapping time  $\tau$  that is proportional to the inverse of the radiation fluence  $\Phi$ :  $\tau = 1/(\Phi\beta)$ , where  $\beta$  is the trapping constant.

**Charge collection efficiency:** one important observable to monitor is the collected charge, which is reported as the most probable value of the cluster charge distribution. The charge collection efficiency (CCE) is defined as the ratio of the most probable value of the cluster charge distribution of a certain point in time against the value before irradiation. The evolution of CCE with luminosity is important to determine the sensor operational voltage: simulations of CCE vs. bias voltage for different radiation fluences are used to assure that the detector is collecting the largest possible amount of signal.

**Signal digitization:** charged particles crossing a detector produce electron–hole pairs that then drift towards the electrodes. The consequent charge induction on electrodes is the so-called *digitization* step in detector simulation.

In Fig. 111 a schematic view of the process flow presented above is shown.

While TCAD can be used for detailed simulations of silicon detectors, it is very demanding in computing time and is not easy to integrate in other tools, for example, Monte Carlo simulations. For this reason, TCAD is often used for the computation of the electric field in silicon sensors, and the resulting

<sup>8</sup>When referring to silicon sensors, the local coordinate  $z$  identifies the direction orthogonal to the collecting electrodes in planar technology and the one parallel to the columns axis in 3D technology.

<sup>9</sup>These defects are deep in the sense that the energy required to remove an electron or hole from the trap to the valence or conduction band is much larger than the characteristic thermal energy  $kT$ , where  $k$  is the Boltzmann constant and  $T$  is the temperature.

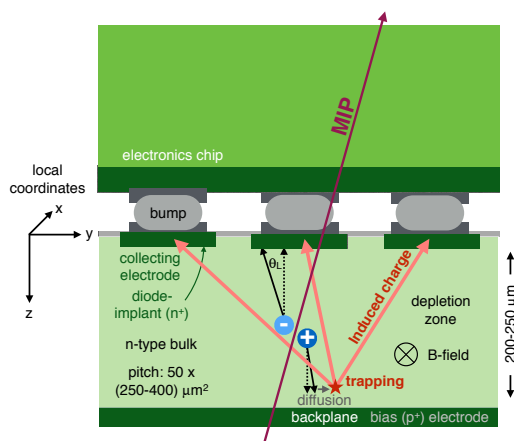


**Fig. 111:** An illustration of the digitization process for planar sensors [3]

field is then fed into other software that include drift-diffusion models of charge carriers, such as AllPix [4], KDetSim [5], and PixelAV [6–8]. AllPix2 [9] in addition allows for simulation of material effects in the experimental set-up such as multiple scattering and nuclear interactions.

Different implementations of sensor simulations are used by the large LHC experiments. In what follows, the implementations for ATLAS (7.1), CMS (7.2), and LHCb (7.3) are described. In Section 7.4 the different strategies of the LHC experiments are compared.

## 7.1 ATLAS

The ATLAS tracking system is described in more detail in Section 3.2. This section will focus on the simulation of radiation effects and charge transport in the sensors in the ATLAS pixel detector. Silicon sensor simulations of the ATLAS SCT are not discussed here.

The ATLAS pixel detector [11–13] contains hybrid pixel modules made by  $n^+$ -in- $n$  sensors bump bonded to custom front-end readout chips. In 2015, the now innermost barrel layer was added to the original detector; this new layer – called the insertable B-layer (IBL) [14, 15] – features thinner sensors (200 vs. 250  $\mu\text{m}$ ) with respect to all other layers as well as smaller cells (50  $\times$  250  $\mu\text{m}^2$ ; everywhere else the pixel pitch is 50  $\times$  400  $\mu\text{m}^2$ ). For more details on the ATLAS pixel detector see Section 3.2.1.1.

As the closest detector component to the interaction point, the pixel detector was subjected to a significant amount of radiation over its lifetime; as stated above, among the barrel layers, the IBL is the closest one to the beam pipe. The total fluence received during its lifetime has been of the order of  $\sim 1 \times 10^{15} \text{ n}_{\text{eq}}/\text{cm}^2$  at the end of Run 2 (corresponding to a luminosity delivered by the LHC of  $159 \text{ fb}^{-1}$ ), while a total fluence of  $1.8 \times 10^{15} \text{ n}_{\text{eq}}/\text{cm}^2$  is estimated by the end of Run 3 in 2023 (for a total estimated integrated luminosity of  $300 \text{ fb}^{-1}$ ). Figure 112 shows the fluence received by the four barrel layers as a function of the number of days since the start of Run 2.

In what follows, the details of a new digitizer model [3] that accounts for effects due to radiation damage will be presented. Section 7.1.1 presents the model used and each component used, and Section 7.1.2 presents the results of the simulation compared with data from Run 2.

### 7.1.1 ATLAS pixel digitizer model overview

In the digitization step [3] energy deposits are obtained from Geant4 [17] and saved in a list of position and energy, called *hits*. Radiation damage effects are modelled in this simulation step for ATLAS Pixel sensors. The algorithm which will be presented here was first developed on AllPix [4], a Geant4-based tool which allows an easy and fast simulation of silicon detector performance after radiation damage.

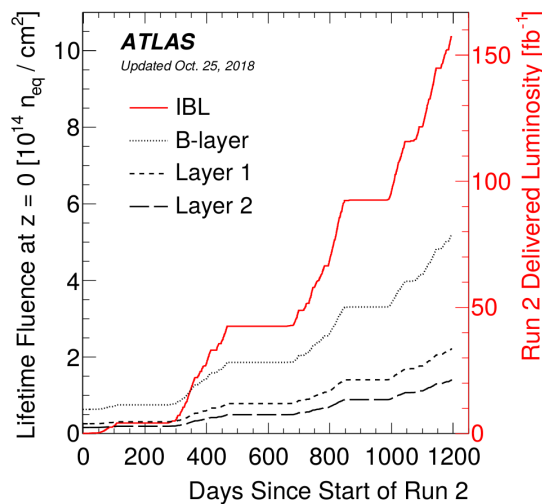


**Fig. 112:** Estimates of the lifetime fluence experienced by the four layers of the current ATLAS pixel detector as a function of time since the start of Run 2 (June 3, 2015) at  $z \sim 0$ . The IBL curve represents both the fluence on the IBL (left axis) as well as the delivered integrated luminosity in Run 2 (right axis). From Ref. [16].

Afterwards, the model was also implemented in the ATLAS common software Athena [18], in order to exploit the full-geometry description of the ATLAS detector, and check what the effects on physical quantities would be. The structure of the main algorithm in the two softwares is very similar.

The algorithm for simulating radiation damage within the ATLAS Athena digitizer is as follows:

- after charge deposition by Geant4, the digitizer takes in as input the charge and position of the various particles, as well as global information such as the electric field profile after radiation damage;
- groups of  $\sim 10$  charges are formed to be treated as a charge chunk to speedup the digitization;
- using the electric field distribution – based on voltage and fluence – the time for the charge chunk to drift to the electrode is evaluated;
- this drift time is compared to a randomly generated trapping time; the final bulk depth for the chunk is hence determined;
- deflections are calculated evaluating the average Lorentz angle along the path (using Eq. 33) and the contribution due to carrier diffusion, hence the final charge chunk position is determined;
- based on the initial and final charge positions, the induced charge on the electrode is then determined using the Ramo potential (Eq. 34).

#### *Geometry and condition configuration*

The first step of the software consists in the loading of all the geometry and operational parameters needed: thickness, pitch, tilt, fluence, trapping time, temperature, and magnetic field strength. Lookup tables are then loaded for Ramo potential, electric field maps, and Lorentz angle maps. Geant4 then generates the energy hits and these are converted into electron–hole pairs; the energy needed is about  $\sim 3.6$  eV for a pair. Charges are then drifted towards the electrodes, and, using the pre-loaded maps, the probability of being trapped is calculated, and then, using the Ramo potential, the induced charge on the electrodes is evaluated.

The different inputs to digitization are described in the following paragraphs.

## Fluence

Fluence is an important input for the simulations, in particular for the electric field determination. Leakage current is the observable used to relate luminosity to fluence. This is obtained from the measurement of leakage current compared with the predictions. Figure 113 (left) shows the predicted leakage current compared with data during Run 2. Figure 113 (right) shows the conversion factor from luminosity to fluence for the IBL, as a function of  $z$ , compared with predictions with Pythia8+ FLUKA [19, 20] and Pythia+Geant4. From a comparison among the different simulations an uncertainty of about 15 % is assumed for this conversion factor.

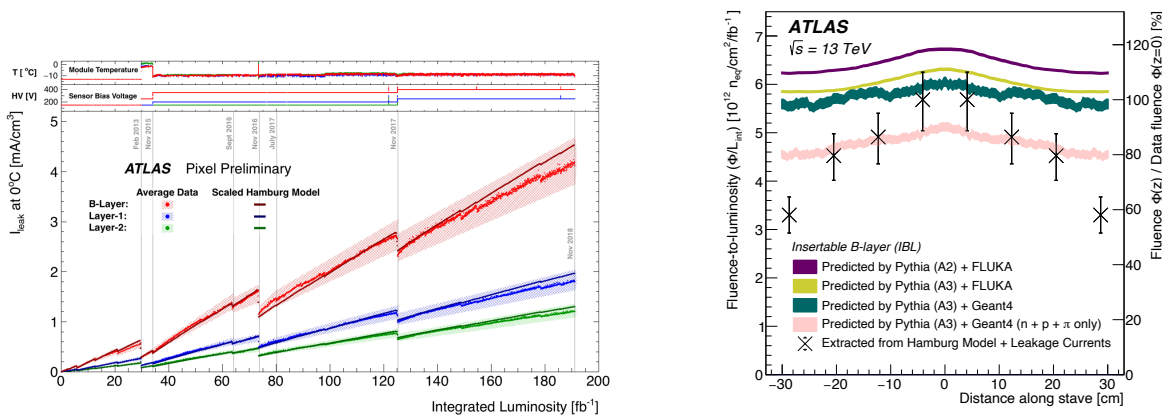


**Fig. 113:** Left: average measured leakage current data of a representative sample of modules in the ATLAS pixel detector barrel layers over the full period of operation. The leakage current data are normalized to  $0^\circ\text{C}$ ; the average module sensor temperature is shown in the top panel. From Ref. [21]. Right: the fluence-to-luminosity conversion factors (extracted from leakage current fits), as a function of  $z$ , compared with the Pythia+FLUKA and Pythia+Geant4 predictions. From Ref. [3].

## Electric field

Once the fluence level is known the electric field profile inside the silicon sensors can be calculated for different bias voltages using TCAD tools. The radiation damage models used in TCAD for simulating the electric field profile in the ATLAS pixel detector were the Chiochia model [22] for planar sensors and the Perugia model [23] for the 3D sensors. The Chiochia model features two traps, with one acceptor and one donor trapping centre, with energy levels at  $E_C - 0.525$  eV and  $E_V + 0.48$  eV for the conduction  $E_C$  and valence band energy level  $E_V$ , respectively. The Perugia model instead includes three trap levels: two acceptor and one donor, with energies:  $E_C - 0.42$  eV,  $E_C - 0.46$  eV, and  $E_V + 0.36$  eV, respectively. As explained in detail in Ref. [3], the values of trap parameters (energy, density, capture cross-sections) were varied to estimate the impact of these uncertainties on the simulated electric field and all the other observables depending on it.

The TCAD simulations are all performed at the temperature indicated by the authors of the radiation damage models used, i.e.,  $-10^\circ\text{C}$  for the planar sensors [22] and  $20^\circ\text{C}$  for the 3D sensors [23]. The reason for this choice is explained in detail for planar sensors in Ref. [3], and the same reasoning applies for 3D sensors. TCAD models only include a small number of effective states, and in reality the temperature dependence is reduced when a more complex (but computationally intractable) combination of states is present. Moreover, when assessing the impact on electric field predictions due to uncertainties from trap parameters as explained above, it was found that a variation of the trap energy level  $E_t$  by 10% of thermal energy  $k_B T$  is consistent with naive temperature variations that bracket all Run 2 operational temperatures ( $-15^\circ\text{C}$  to  $+20^\circ\text{C}$ ) [3]. Therefore, the impact on electric field prediction due to uncertainties from imperfect temperature-dependence parameterization in TCAD radiation damage models is already taken

into account by variations of values of TCAD radiation damage model trap parameters.

In order to save simulation time, many quantities derived from the electric field (such as the time for a charge to drift to an electrode) are also precomputed and saved as maps. Further details can be found in Ref. [3]. The two main parameters for generating maps are the fluence and the bias voltage. Typically, the electric field is computed only for a few benchmark pairs as it is not feasible to precompute all possible combinations. To be as flexible as possible, a new method has been developed to produce electric field maps for any (fluence, voltage) pair on the fly within the digitizer by interpolating existing electric field maps. This takes advantage of the fact that the electric field at a fixed sensor depth varies smoothly with fluence and voltage. Given a desired (fluence, voltage) pair an interpolation with cubic splines is first among available fluences to obtain various samples with the correct fluence but different voltages. Using these new samples the interpolation is repeated, this among voltages, to obtain the correct (fluence, voltage) target. Closure tests on this interpolation method were performed by comparing the precomputed maps with the interpolated maps. Example distributions of the electric field and  $dE/dx$  in Figure 114 show good agreement between the two. The electric field interpolation has now been added to the Athena [18] digitizer for planar sensors.

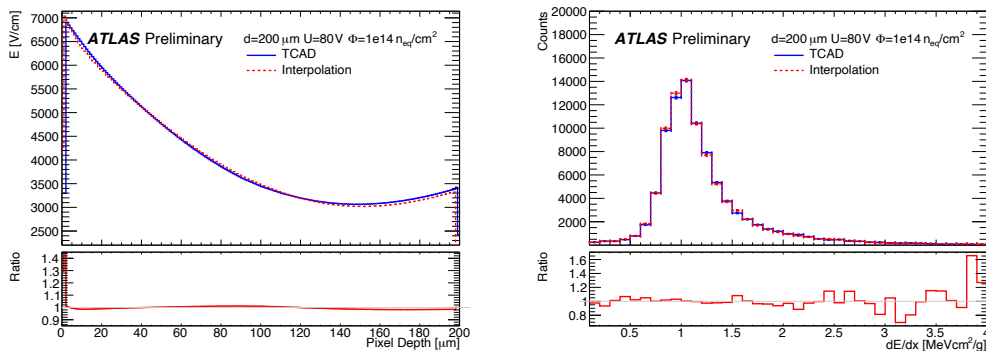


**Fig. 114:** Comparisons of the electric field and stopping power  $dE/dx$  for the interpolated maps and the maps generated directly from TCAD [24].

In addition to the more common planar pixel sensors, ATLAS also has 3D pixel sensors located at high  $\eta$  in the IBL. A radiation damage implementation for 3D sensors has been added to Athena too. The implementation is very similar to that of the planar sensors, despite the differing geometry.

To validate the Athena implementation muons have been simulated hitting the 3D sensors (with the planar sensors disabled). The simulated average  $dE/dx$  is plotted for a series of benchmarks, with fluences ranging from 0 to  $10^{16}$   $n_{eq}/cm^2$ . Figure 115 shows that the results from Athena agree well qualitatively with the results from standalone AllPix simulation, which itself has been validated against real test beam data.

### Lorentz angle

In the simulations, the Lorentz angle is calculated according to Eq. 33 and saved in maps which are loaded at the beginning for each geometry and condition set-up (fluence, bias voltage, and temperature).

The Lorentz angle has a direct impact on the cluster size, and it is therefore an important parameter to monitor. The Lorentz angle is obtained by fitting the transverse cluster size as a function of the incidence angle of the associated track, with a function  $F$  defined as:

$$F(\alpha) = [a \times |\tan \alpha - \tan \theta_L| + b/\sqrt{\cos \alpha}] \otimes G(\alpha|\mu = 0, \sigma), \quad (35)$$

where  $\alpha$  is the track incidence angle with respect to the normal direction of the sensor in the plane perpendicular to the magnetic field. The parameter  $\theta_L$  is the fitted Lorentz angle,  $G$  is a Gaussian prob-

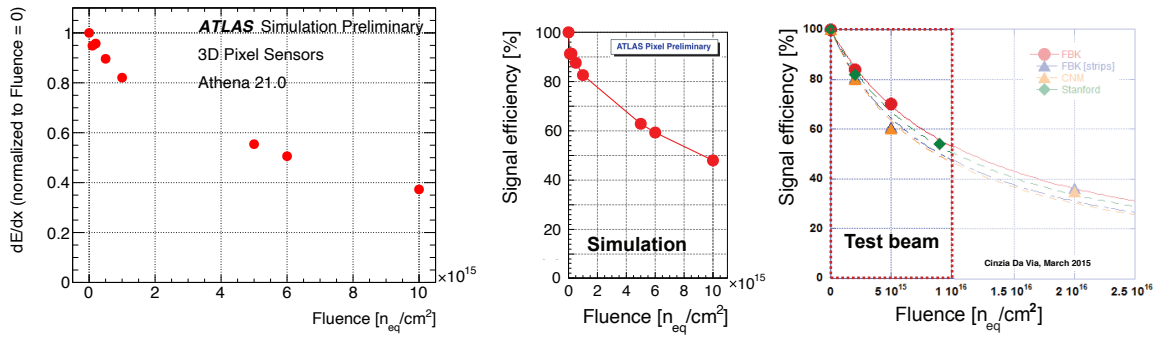


**Fig. 115:** Comparison of the charge collection efficiency vs. fluence for (left) the Athena simulation [25], (mid) the standalone AllPix simulation [26], and (right) real test beam data [27, 28].

ability distribution evaluated at  $\alpha$  with mean 0 and standard deviation  $\sigma$ , and  $a$  and  $b$  are two additional fit parameters related to the depletion depth and the minimum cluster size, respectively.

Figure 116 shows the mean transverse cluster size versus track incidence angle, in both data and AllPix simulation for integrated fluence at the end of 2016 and bias voltage of 80 V.

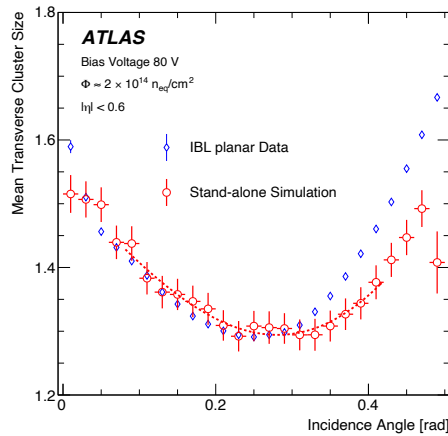


**Fig. 116:** The mean transverse cluster size versus transverse incidence angle near the end of the 2016 run (with about  $\sim 2 \times 10^{14}$   $n_{eq}/cm^2$  collected) with a bias voltage of 80 V compared with simulations from AllPix using the Chiochia model. From Ref. [3].

### Charge trapping

The trapping constants, i.e., the  $\beta$  values, have been taken from different measurements. It has been found that  $\beta$  depends on the type of irradiation, the temperature, and the annealing history, and on carrier type ( $e$ ,  $h$ ). The values used in the digitizer are an average from Refs. [29–31], with the uncertainties that account for differences in central value, irradiation type, and thermal history. The values used were:

$$\begin{aligned}\beta_e &= (4.5 \pm 1.5) \times 10^{-16} \text{ cm}^2/\text{ns}, \\ \beta_h &= (6.5 \pm 1.5) \times 10^{-16} \text{ cm}^2/\text{ns}.\end{aligned}$$

### Ramo potential and induced charge

Ramo potential maps are loaded at the beginning of each simulation, one for each geometry, and are used whenever a charge is trapped to estimate the induced charge in all the pixels in a  $3 \times 3$  matrix around the

closest pixel to the trapping position. These maps are evaluated with TCAD in order to solve the Poisson equation. Figure 117 shows a 2D projection of the Ramo potential for an IBL planar sensor.

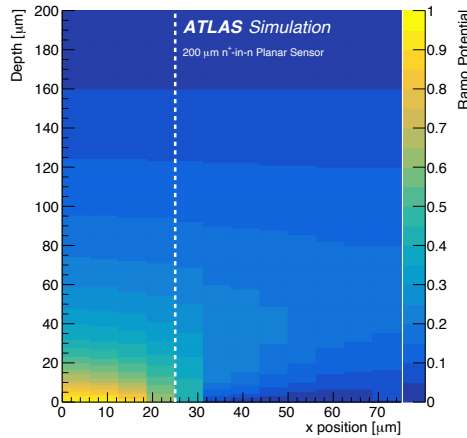


**Fig. 117:** A 2D projection in the  $z - x$  plane of the Ramo potential map for an ATLAS IBL planar module. The dashed vertical line (at  $25 \mu\text{m}$ ) indicates the edge of the primary pixel. From Ref. [3].

### 7.1.2 Validation with data

The evolution of the main performance parameters with fluence is simulated with AllPix, and the results are compared with collision data. This software is also used to predict future condition of the detector, in order to plan changes in the set-up to assure a high detection efficiency. In this section results obtained during the Run 2 with ATLAS detector are presented, in particular for the IBL system. During this time the bias voltage was increased to cope with radiation damage: the IBL sensors have been operated at 80 V in 2015, 150 V in 2016, 350 V in 2017, and 400 V in 2018.

In the following, the comparison between data and simulations is presented for charge collection efficiency (Section 7.1.2.1) and Lorentz angle (Section 7.1.2.2); results for mobility modelling are included too (see Section 7.1.2.3).

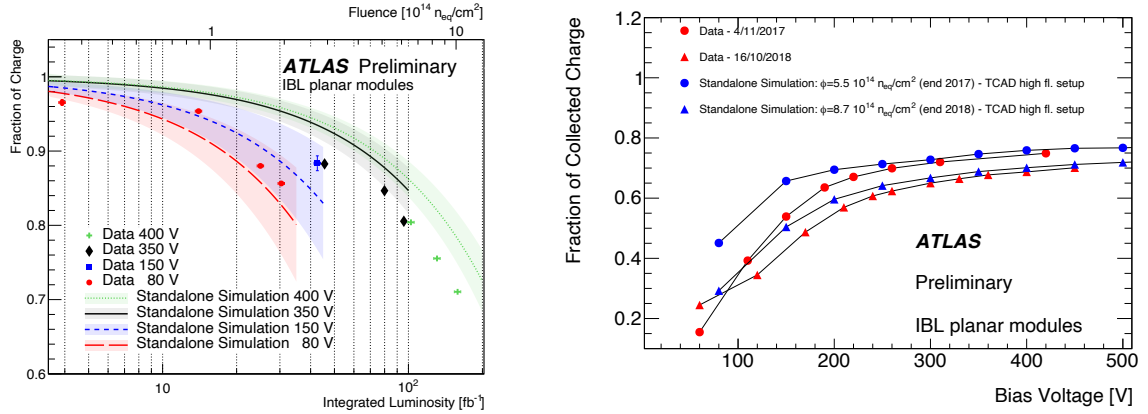
#### 7.1.2.1 Charge collection efficiency

Figure 118 (left) shows the charge collection efficiency as a function of the delivered luminosity for central ( $|\eta| < 0.8$ ) IBL modules. Systematic uncertainties include fluence calculation and variation of the TCAD model and trapping parameters (simulations) and the drift in the charge calibration (data). Within uncertainties, the data and simulations are in agreement.

Figure 118 (right) shows the evolution of the collected charge as a function of the bias voltage in the IBL modules. Data and simulations are shown for the end of 2017 and 2018 for IBL modules. The data were taken in special runs where scans of bias voltages were performed. Again the simulation is in good agreement with data, both in trend and absolute value.

#### 7.1.2.2 Lorentz angle

The dependence of the Lorentz angle on fluence was simulated using the AllPix [4] package, with electric field maps produced using TCAD simulations based on the Chiochia radiation damage model [22]. Figure 119 shows the comparison of the Lorentz angle values obtained from a  $Z \rightarrow \mu\mu$  sample with the simulation. The vertical error bars on the data points represent the statistical uncertainties, while the error bars on the simulated points represent the statistical and systematic uncertainties on the simulation, obtained from variations on the simulated parameters [34].



**Fig. 118:** Left: charge collection efficiency as a function of luminosity [3]. Right: charge collection efficiency as a function of bias voltage [32].

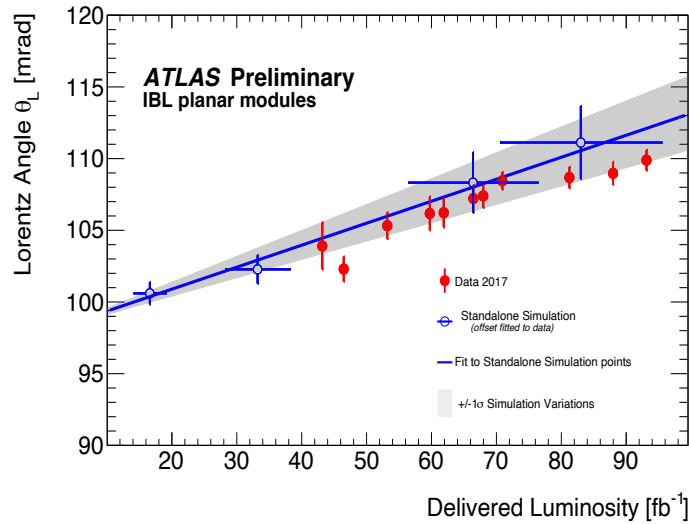


**Fig. 119:** Comparison of the evolution of the Lorentz angle with luminosity in data (red points) and in simulation (blue points) [34].

The slope of the linear fit in Fig. 119 is obtained from the simulated points, while the intercept is fitted from the data. A good agreement is observed between the data and the simulation within the uncertainties.

### 7.1.2.3 Mobility studies

The mobility  $\mu$  is defined as the ratio between the drift velocity of charge carriers in a silicon module and the electric field. As anticipated above, mobility is a function of temperature and electric field, and can be related to the value of the Lorentz angle by the value of the magnetic field

$$\tan \theta_L \sim \mu |\vec{B}|. \quad (36)$$

Thus, correctly modelling the Lorentz angle is equivalent to a good modelling of the mobility in the Monte Carlo simulation. Comparisons of the measured Lorentz angle with the Monte Carlo simulations during Run 1 showed discrepancies of about 10% on the value of  $\theta_L$  [37], so an investigation of the mobility models implemented in the simulations was carried out, with the goal of improving the data-MC agreement for Lorentz angle. At low electric fields, the mobility can be parameterized as a power

law of the temperature

$$\mu(T) = aT_n^{-b}; \text{ where } T_n = \frac{T}{300\text{K}}, \quad (37)$$

while the extrapolation to higher electric fields can be parameterized using the Thomas model [35]

$$\mu(T, E) = \mu_0(T) \left[ 1 + \left( \frac{\mu_0(T)E}{\nu_s(T)} \right)^\beta \right]^{-\frac{1}{\beta}}. \quad (38)$$

The parameters  $a$  and  $b$ , considered for the low-field parameterization in Eq. 37 can be found in Table 13 for both electrons and holes, while the parameters  $\nu$  and  $\beta$  for the high field extrapolation in Eq. 38 are summarized in Table 14 as a function of the temperature [37].

**Table 13:** Parameters for the low-field mobility parameterisation in Eq. 37

Low-field model	Parameter	Electrons	Holes
Jacoboni–Canali [38]	$a$ [cm <sup>2</sup> /(V·s)]	1533.7	463.9
	$b$	2.42	2.20
Canali [36]	$a$ [cm <sup>2</sup> /(V·s)]	1437.7	463.9
	$b$	2.42	2.20
Hamburg–Thomas [39]	$a$ [cm <sup>2</sup> /(V·s)]	1440(15)	474(10)
	$b$	2.260(7)	2.619(7)

**Table 14:** Parameters for the high-field extension of the mobility models, following the Thomas model in Eq. 38.

Extended model	Parameter	Electrons	Holes
Jacoboni–Canali [38]	$\nu_s$ (cm/s)	$1.07 \times 10^7 \times T_n^{-0.87}$	$8.34 \times 10^6 \times T_n^{-0.52}$
	$\beta$	$1.109 \times T_n^{0.66}$	$1.213 \times T_n^{0.17}$
Canali [36]	$\nu_s$ (cm/s)	$1.00 \times 10^7 \times T_n^{-0.87}$	$8.34 \times 10^6 \times T_n^{-0.52}$
	$\beta$	$1.109 \times T_n^{0.66}$	$1.213 \times T_n^{0.17}$
Hamburg [39]	$\nu_s$ (cm/s)	$1.054(38) \times 10^7 \times T_n^{-0.602(3)}$	$9.40(27) \times 10^6 \times T_n^{-0.226(2)}$
	$\beta$	$0.992(4) \times T_n^{0.572(3)}$	$1.181 \times T_n^{0.644(3)}$

A study of the different mobility models for unirradiated modules was performed using 2015 data. The results of the simulations using the models summarized in Tables 13 and 14 are compared with the data from the ATLAS Insertable B-Layer (IBL) in Fig. 120. Results show discrepancies between the data and the simulation using the Jacoboni–Canali model, while the Canali and Hamburg–Thomas models give a good description of the data.

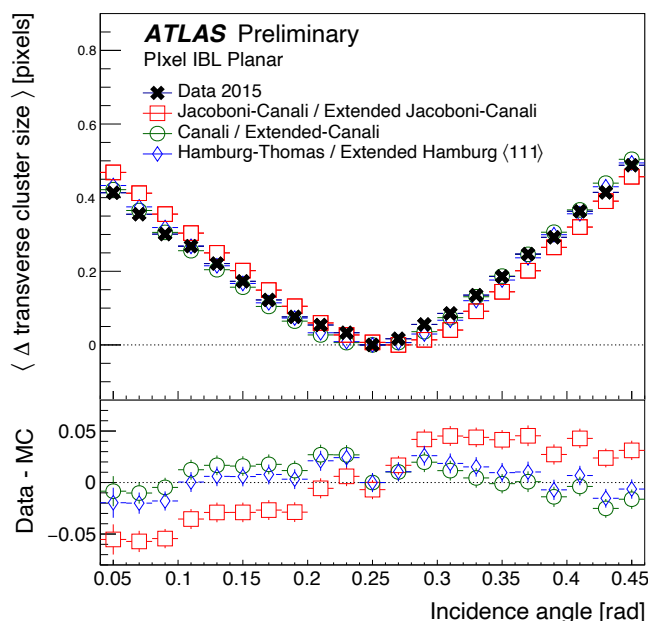


**Fig. 120:** Distribution of the cluster transverse size as a function of the incidence angle for data and different mobility models. The Jacoboni–Canali model shows important discrepancies with the data. From Ref. [37].

### 7.1.3 Summary

As the closest detector system to the interaction point, the ATLAS pixel system receives the most radiation fluence and dose. By the end of Run 2 the IBL sensors received an integrated radiation fluence up to  $10^{15}$  (1 MeV)  $n_{\text{eq}}/\text{cm}^2$ . The effects of radiation damage are being observed and measured, such as decreasing signal size and drifts in the Lorentz angle. A digitizer model implemented by ATLAS has been presented which models the effects of radiation damage [3]. It is based on Geant4 and uses TCAD simulation results as inputs for the electric field. Comparisons with data show reasonable agreement. These simulations help to make decisions about the operating working point for the future data taking period in order to ensure good online and offline performance of the ATLAS pixel detector, and to guide the design of the future detector at the HL-LHC.

For future ATLAS physics in Run 3 and the HL-LHC, understanding radiation damage effects will be crucial. The radiation damage digitizer will be a default component of the ATLAS simulations, helping to make accurate performance predictions with increasing luminosity. Future challenges include deciding the exact fluences to use as simulation inputs, and also ensuring that the digitizer will run fast enough for simulation production.

## 7.2 CMS

This section describes the modelling of the charge generation and transport in the silicon sensor of both the CMS pixel and CMS strip detector. Both systems have been described in more detail in Section 3.2.2.

### 7.2.1 CMS pixel detector

The CMS pixel detector uses  $285\ \mu\text{m}$  thick  $n^+$ -in- $n$  sensors with  $100 \times 150\ \mu\text{m}$  pixels. The sensors are estimated to be  $-14\ ^\circ\text{C}$  to  $-8\ ^\circ\text{C}$  when powered. The operational bias voltages at the end of Run 2 ranged from 250–450 V as shown in Table 2 in Section 3.2. For this detector, the modelling of radiation damage to the silicon sensors is performed with the standalone simulation software PixelAV [6–8] that is independent from the full CMS simulation framework CMSSW [40].

The detailed sensor simulation PixelAV simulates the passage of a pion ( $\pi$ ) through the sensor and incorporates the following elements:

- **charge deposition:** an accurate model of charge deposition by primary hadronic tracks uses the ‘exact’  $\pi - e$  elastic cross-sections of Bichsel [41], that depend on the electron energy, to determine the  $\pi$  mean free path. It takes into account the number of electron–hole pairs produced when the scattered electrons or ‘delta rays’ lose energy. The total number of electron–hole pairs is chosen from a Poisson distribution where the mean number of pairs is determined assuming that it takes 3.68 eV to produce a pair. The delta rays are propagated until they lose all energy or they leave the sensor;
- **electric field:** a realistic three-dimensional electric field profile resulting from the simultaneous solution of Poisson’s equation, carrier continuity equations, and various charge transport models is generated with the TCAD package. With as input the pixel cell geometry and material properties, TCAD predicts a non-uniform spatial distribution of space-charge density for computing charge propagation inside the sensor bulk. A temperature of 263 K was assumed in TCAD simulations;
- **charge transport:** the electrons and holes produced by the primary hadron drift to the sensor implants under the influence of the internal electric field and the external magnetic field. Charge carriers are transported by integrating the equations of motion:

$$\frac{d\vec{x}}{dt} = \vec{v} \quad (39)$$

$$\frac{d\vec{v}}{dt} = \frac{e}{m^*} \left[ q\vec{E} + qr_H\vec{v} \times \vec{B} - \frac{\vec{v}}{\mu(E)} \right]. \quad (40)$$

The electrons and holes drift with a carrier-dependent mobility ( $\mu$ ) that depends on the electric field ( $E$ ) and temperature. Here, the effective masses  $m^*$  are  $0.260 \cdot m_e$  for electrons and  $0.241 \cdot m_e$  for holes in silicon;

- **charge trapping:** when charge carriers are trapped they are captured for periods of time that are long as compared with the integrating time of the pre-amplifiers and are not detected with full efficiency. This trapping time is incorporated in the simulation by halting the propagation of that charge carrier according to the effective trapping times measured in Ref. [30]. The trapping constants used for electrons and holes in CMS simulation are tuned to measurements from data;
- **charge collection efficiency:** after all charge carriers have reached the boundary of the detector or have been trapped, the program counts the number of electrons that have been collected by each  $n^+$  implant. Then it calculates the additional charge induced on each pixel by trapped electrons and holes by approximating the detector as a parallel plate capacitor with a rectangular segment anode.

For each event, the simulation outputs the coordinates of the pion entry and direction, the generated number of electron–hole pairs, and two sets of signals for a pixel array. The first set includes only collected electrons and the second set includes collected electrons and induced signals from trapped charge. The final step consists in a simplified simulation of the electronics and readout system. First, a random noise is added to each pixel signal. Then, a function that simulates the analogue response of the ROC is applied to the total signal. The results of the PixelAV simulation are employed in the event reconstruction step of CMSSW. This is done by applying corrections from templates stored for sets of track angles and cluster charges to the total deposited charge in simulation and further correcting the position of the reconstructed pixel hit.

**Template reconstruction:** the PixelAV simulation was originally written to interpret beam test data from several un-irradiated and irradiated sensors. In CMS, the simulation is used to produce cluster projection shapes, also called ‘templates’, across measured cluster projections [42]. These templates are produced for different incident track angles ( $\cot \alpha, \cot \beta$ ) and hit positions defined with grids of eight

slices in local  $x$  and  $y$  coordinates within a pixel. They take into account the sensor geometry and are produced under certain conditions of fluence, temperature, bias voltage, and magnetic field. A single cluster template is created by repeatedly simulating the particle traversal for a certain incidence angle and position within a pixel using the PixelAV software. Parameters in PixelAV were originally taken from Ref. [22]. However, CMS has developed techniques to tune the PixelAV trapping parameters, as well as the TCAD donor and acceptor concentrations and the electron and hole trapping rates therein, from collision data through measurements of the charge collection vs. depth. The templates produced from the tuned PixelAV simulation are used to find the best fit and hence an estimate of the in-pixel hit position in both  $x$  and  $y$ . A template contains:

- the charge distribution in  $x$  and  $y$  for a charge bin;
- the average and maximum signals in the  $x$  and  $y$  projections as well as the expected RMS of the average signals;
- the averages of the minimum  $\chi^2$  functions in  $x$  and  $y$  to be used in the calculation of goodness of fit probabilities of in-pixel hit position and signals;
- the average correction to the average residuals to correct for effects like charge migration or signal fluctuating above or below readout threshold.

These templates were produced about every few  $\text{fb}^{-1}$  just after installation, when type inversion occurs, and later about every  $10\text{fb}^{-1}$  following periods of annealing or changes in detector parameters after calibration. This amounted to about twelve updates in the templates in a year. The templates are not only used to compute in-pixel hit position, but are also used to reweight the digitized cluster charge profile as a function of the production depth.

**Corrections in the pixel hit reconstruction:** the template-based reconstruction algorithm aims to get a better estimate of the pixel hit position by accounting for the charge sharing functions of the detector and how they are modified during large portions of its useful life. This is possible through the use of the projected pixel information stored in a template. The technique is based on fitting the now measured pixel cluster  $X$  and  $Y$  projections to the pre-determined cluster shapes or templates produced with PixelAV. Given a track with angles  $\alpha$  and  $\beta$  incident to the pixel module, the pre-determined cluster template is compared to the actual cluster produced by the track in question. A  $\chi^2$  minimization is performed with hit  $X$  and  $Y$  positions as floating variables. The in-pixel hit position is given by the  $X$  and  $Y$  coordinates which minimize the  $\chi^2$  comparison.

The cluster template technique was originally developed to optimally estimate pixel hit positions after radiation damage, but it was found that it performs better than standard CMS pixel hit reconstruction [43] even before irradiation [42]. The technique requires knowledge of the track direction, so it is used in the second pass of pixel hit reconstruction, when track incidence angles on detector modules are known. In the first pass of the reconstruction the standard technique is used. Results of this method are detailed in Ref. [44].

**Pixel cluster charge re-weighting** The pixel charge profile is defined as the normalized average pixel charge as a function of the production depth. For a non-irradiated, fully depleted detector, the pixel charge profile is expected to be flat as the detector is fully efficient and all the charge is collected. For an irradiated detector, on the other hand, charge collection losses are expected due to the trapping of carriers. The losses are larger for the charges released further from the readout plane. This behaviour is shown in Fig. 121 for different accumulated integrated luminosities during the data taking in 2017–2018. During the 2017 Extended Year-End Technical Stop, the barrel pixel detector was held at temperatures above  $10^\circ\text{C}$  for 53 days. The beneficial effect of the annealing during this period is clearly visible in the flattening of the pixel charge profile. At the beginning of 2018 data taking, the charge collection was additionally increased in Layer 1 by raising the bias voltage from 350 V to 400 V.

The cluster charge re-weighting (CCR) algorithm attempts to describe the effects of radiation damage and annealing. This algorithm modifies the charges in a cluster arising from a single simulated

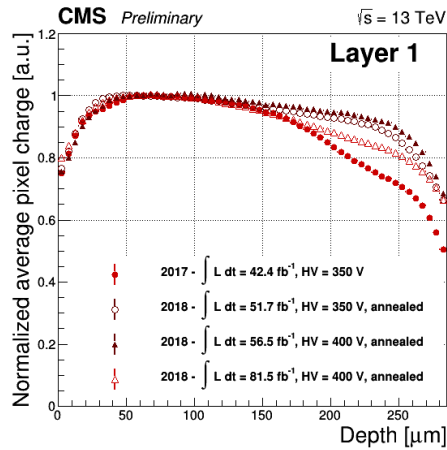


**Fig. 121:** Average pixel charge as a function of production depth [45]. The charge distribution is shown for the Layer 1 of the CMS barrel ip detector at the end of 2017 ( $HV = 350$  V), at the beginning of 2018 data taking ( $HV = 350$  and  $400$  V), and after  $30.0 \text{ fb}^{-1}$  of data collected in 2018. The selection includes tracks with  $p_T > 3$  GeV, pixel cluster charge  $< 1000 \text{ ke}^-$ , cluster size in  $y < 4$ , and hit position residuals  $< 100 \mu\text{m}$ .

hit such that a better description of the sensor response is obtained, while maintaining the randomized nature of the signal creation process. The method of CCR sets in at the end of the first part of the digitization process and is applied to clusters of pixel charges resulting from a single primary particle. Therefore, in CMSSW, the CCR is implemented before the charges in the pixels are summed and thresholds are applied, but after the cluster finding step.

To apply the CCR to a simulated cluster, the incidence angle and position of the corresponding primary particle and the module ID are used to find the most suitable cluster templates from the set of PixelAV templates. These are generated for various incidence angles and positions, as well as for different levels of irradiation. The templates are read from a database, and an interpolation is performed between the simulated particle parameters. The original  $x,y$  induced charge of a pixel in the cluster is then scaled with the ratio  $w$  of the template pixel charges at the same position inside the cluster for an irradiated ( $t^{\text{irr}}$ ) and an un-irradiated sensor ( $t^{\text{unirr}}$ ). A matrix of  $13 \times 21$  pixels is defined, which covers the full cluster and has the particle hit position in its centre. For any pixel, specified by its pixel coordinate  $(x, y)$  with respect to the lower left pixel of this matrix, the reweighted charge signal  $x,y$  is determined as

$$\text{signal}_{x,y} = \frac{t^{\text{irr}}_{x,y}}{t^{\text{unirr}}_{x,y}} \times \text{original}_{x,y}. \quad (41)$$

For pixel charges of the templates below a track-angle-dependent minimum charge<sup>10</sup>, no weights are computed, and instead the pixel charge is computed using the weight of the closest pixel with a weight.

One way to verify the effect of the CCR is to extract the collected charge as a function of the charge carrier creation depth from very long clusters. For unirradiated sensors, this profile is flat, and it is tilted for strongly irradiated sensors, as shown in Fig. 122. In the same figure, a preliminary distribution of the average charge profile shows that the CCR can reproduce this effect.

**Conclusion** The PixelAV simulation was developed to model pixel sensor physics as accurately as possible but its speed is not optimized to be included as part of the main CMS simulation framework. Therefore, its usage is limited to estimate the radiation damage effects in a standalone mode. Specifically,

<sup>10</sup>This helps to suppress low-charge clusters resulting from secondary electrons.

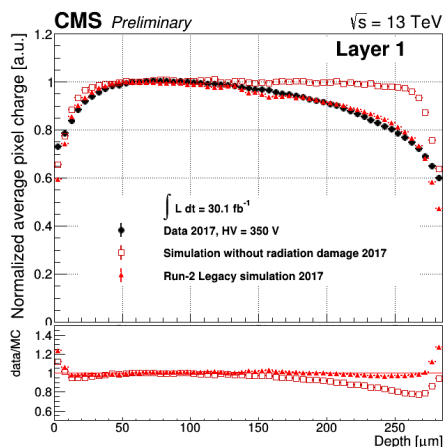


**Fig. 122:** Average pixel charge as a function of production depth for the Layer 1 of the CMS pixel barrel detector in 2017 [46]. The profile of the data collected (black) shows the losses expected due to the trapping of carriers as a function of depth. The charge simulation without the CCR algorithm is flat and shown in red squares. After applying the CCR algorithm a more accurate description of the simulated charge profile can be seen in red solid triangles.

it provides a more accurate estimate of the pixel hit position in the event reconstruction and is used to implement corrections to the simulated pixel cluster charge profiles. The latter is performed through a reweighting algorithm that includes more realistic modelling and irradiation effects. The simulation and the reconstruction are currently being synchronized by using templated cluster shapes generated from the same models. Preliminary cluster profiles measured in data and simulation show encouraging and promising results that reflect a more accurate estimate of the radiation damage effects.

### 7.2.2 CMS strip tracker

The CMS strip tracker has been in operation since the start of CMS in 2009. The strip sensors are of n-type silicon with  $p^+$  single-sided strips with a thickness of  $320 \mu\text{m}$  up to a radius of  $600 \text{ mm}$ , and  $500 \mu\text{m}$  at larger radii.

For the case of CMS strip tracker, the Geant4 package that describes the energy loss in the CMS tracker based on the interactions between the incoming particles and the bulk of the silicon sensor is not sufficient to simulate the signal collected in the real detector. For the proper modelling of radiation damage in the CMS strip tracker, an experiment-specific simulation of the signal and noise is required. This has been implemented within the CMS Software framework (CMSSW).

**Simulated hits:** for a given silicon strip module whose geometry is known, the simulation [47] starts from Geant4 hits providing information about the direction of the incoming particle, a hit position in the local coordinate frame and the total energy loss. The first step consists in dividing the trajectory of the incoming particle and randomizing the energy loss in each sub-path following a Landau distribution. The second step simulates the charge carrier drift including thermal diffusion. The underlying hypotheses are that the  $E$ -field is normal to the sensor plane and that there is no charge collection inefficiency. The next step emulates the effect of the inter-strip capacitance which induces charges on neighbouring strips of the one collecting the charge carriers. This is performed through a parameterization of the cross-talk effect assuming that for a given charge  $Q$  collected on a strip  $i$ , the signal observed on that strip will be  $x_0 \times Q$ , the two closest strips  $i \pm 1$  will measure a charge  $x_1 \times Q$  and the second ones ( $i \pm 2$ ) a charge  $x_2 \times Q$ . The parameters are constrained by the relationship  $x_0 + 2x_1 + 2x_2 = 1$ . The parameterization depends on the detector geometry and the readout mode of the APV25 (peak or deconvolution). To simulate the front-end electronics, a parameterization of the pulse shape is provided for both readout modes. It is

assumed that the detectors are synchronized and that the signal of ultra-relativistic particles are sampled at their maxima. Consequently, the signals collected for low  $\beta$  particles, loopers, as well as out-of-time pile-up effect induced by the electronic response are properly simulated. The above described simulation chain produces simulated hits (**SimHits**).

**Data digitization:** the next goal consists in simulating the digital data acquired by the back-end electronics (front-end driver, or FED), called the **digis**. Contributions from all particles, including in-time and out-of-time pileup, are taken into account. A list of bad components is extracted from an offline database and is used to suppress the signal for the corresponding channels. In order to describe the noise, it is required to randomize the summed signal according to the knowledge of the noise in each channel. The noise is also stored to and retrieved from a database. To simulate the optical chain response where gains vary between links, values of gains per APV stored in the database are used. The last elements in the readout chain are the FED where the digitization, a zero suppression and a cluster algorithm are performed. The signal processing in the FED is emulated in the CMSSW framework leading to 8-bit digis as provided by the FEDs during data-taking.

**Measurements in data:** to be as realistic as possible, quantities extracted from measurements in data are used to store estimates of observables in a database. During Run 2, the bad component list, the noise, the gains, the cross-talk parameters, and the APV signal shape were measured. These measurements have been used to either feed the database or to update parameters stored in configuration files. The noise is measured simultaneously with the pedestals during calibration runs where no collisions occur. The APV signal shape is measured with charge injection to estimate the electronic response. To simulate the observed signal, however, it has been required to convolute it with a physical signal simulated with external tools. The gains of the optical chains are measured using a reference signal with a fixed amplitude that marks the end of optically transmitted data words, called tickmark, in dedicated runs. The cross-talk parameters have been measured in cosmic runs both without magnetic field to avoid Lorentz deflection, as well as in non-zero-suppressed data-taking mode in order to avoid threshold effects.

All these quantities evolve with time and are updated accordingly. In order to validate the simulation, data/MC comparisons have been performed focusing on the most relevant quantities, mainly the cluster charge and width.

**Cluster charge:** The cluster charge is in general very well reproduced as a result of well-described gains. In the latest simulation campaign of the full Run 2 data, a simulation of the preamplifier has been introduced. It simulates the non-linear response of the pre-amplifier of the APV that was observed early in Run 2 (for a more detailed description of the effect, see Section 6.2.2). This effect is now propagated into the simulation and especially improves the description of the low charge contributions.

**Signal:** an improved description of the APV signal was achieved mainly with a reparameterization of the electronics. The change in the signal description in the simulation impacts the description of off-time signals such as out-of-time pileup and particles with a time of flight similar to that of a photon. The noise decreased with change of the operating temperature, that was changed from  $-15^{\circ}\text{C}$  to  $-20^{\circ}\text{C}$  at the start of 2018, but increased with irradiation. A new description of the noise improved the description of a drop in the signal-over-noise ratio that was measured in the data. This is shown on the left of Fig. 123. The improved noise description also has an impact on off-track clusters and the low charge description of the on-track clusters.

**Cross-talk:** cross-talk is related to the inter-strip capacitance which is affected by surface damages and depends on bias voltage. A comparison of the parameters for the barrel detectors are shown on the right in Fig. 123. The cluster width description has significantly been improved thanks to a new measurement of cross-talk parameters. While discrepancies still remain, they do weakly impact downstream quantities. The optical link gain decreased with time due to a loss of efficiency in the AOH and a loss of transparency in the optical fibres. The update of the gains helps to better describe the fraction of channels having signal saturating the 8-bit ADC.

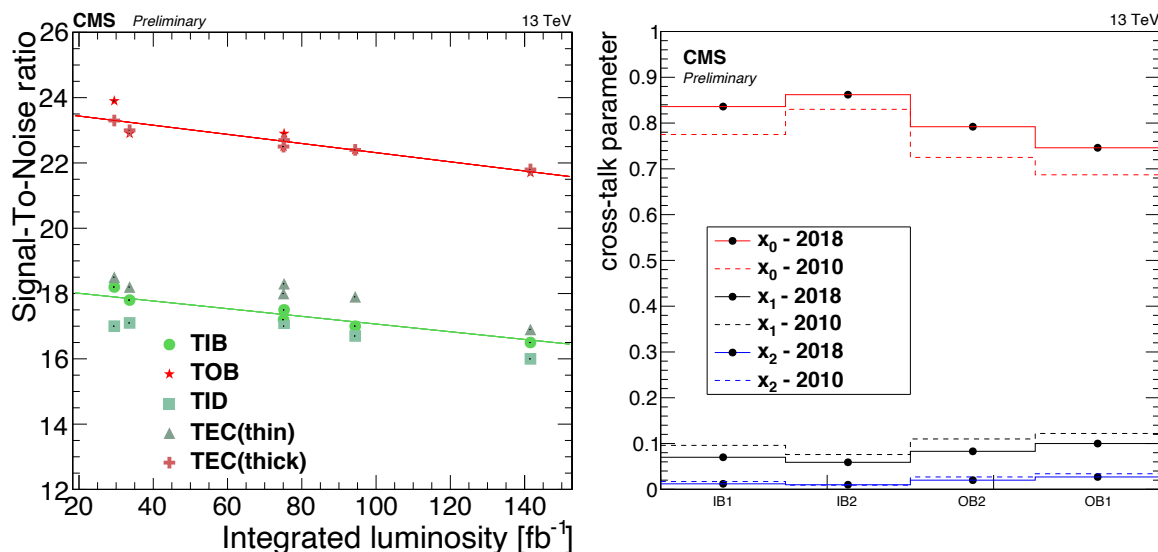


**Fig. 123:** Left: the evolution of the signal-over-noise ratio for modules belonging to different partitions [48]. Higher ratios correspond to the thick ( $500\ \mu\text{m}$ ) sensors. Right: cross-talk parameters for the four barrel silicon strip sensor geometries measured in Run 1 and Run 2 [49].

**Hit efficiency:** measurement of the hit efficiency as function of the pileup shows a linear dependence. The source of inefficiency has been identified as originating from heavy ionizing particles (HIP), or from inelastic nuclear interactions within the active volume. The inefficiency does not exceed 2% even at high pileup and for innermost layers. A simple approach to simulate inefficiency exists in the simulation but has not been used in the latest simulations.

**Conclusion:** the tracker simulation has been improved using the best knowledge we have on the detector through new measurements of observables and corresponding updates of the database and parameters. Moreover, a simulation of the preamplifier has been developed mainly to better describe the data in the first periods of 2016 where the silicon strip tracker suffered from dynamic inefficiencies. Beyond similar measurements that will need to be performed during Run 3, two kinds of further improvements could be foreseen. The inclusion of the HIP-induced hit inefficiency could be used in production. Moreover, as the detector will suffer even more from irradiation, a drop of charge collection efficiency is expected to be observable in the innermost layer. After a dedicated measurement, this effect could be injected into the simulation to even better describe the signal-over-noise ratio.

In general, the validation of the simulation shows that the track reconstruction and downstream algorithms are quite robust and do not require a very fine level of accuracy in the simulation.

### 7.3 LHCb

A more detailed description of the LHCb VELO detector is given in Section 3.2. The LHCb VELO detector has n-on-n silicon sensor pairs of  $300\ \mu\text{m}$  thick. Each of the sensor pairs provides a single 3D measurement by employing both radial and concentric strip topologies, with a sensor pitch ranging from  $35\ \mu\text{m}$  closest to the beam line to  $101\ \mu\text{m}$  further away from the beam line. These innermost VELO sensors at 8 mm from the proton beams during stable beam conditions have seen fluences up to about  $\Phi_{\text{eq}} \sim 6.5 \times 10^{14}/\text{cm}^2$ . High-quality simulation is of major importance for LHCb experiment. The overall strategy is identical to each subdetector that exploits silicon-based devices and may differ in some details related mainly to the emulation of the readout electronics. The full processing chain leading to the production of simulated samples is divided into three independent stages:

1. generation of proton–proton interaction with a particular final state particles and their propagation through the detector (simulation phase);
2. simulation of the detector response (digitization phase);
3. detector output data decoding, track finding and fitting (reconstruction phase).

In the first and most time-consuming stage, the full truth information (a particle 4-momenta and its identification) is used by the LHCb Gauss application [50] to simulate the effects of the passage of particles through detector material. Gauss is interfaced with Geant4 [51] package that is dedicated to simulating with great precision effects such as energy loss or multiple scattering. The results are then stored in a specialized class called MCHit. The next stage, performed by the LHCb application Boole [52], uses the MCHit objects to perform the detector response simulation (see *Digitization* below). In addition, the output of Boole is formatted in an identical way it is sent out to processing in the trigger farm by the respective detectors. Finally, the LHCb Brunel application [53], simulating the full reconstruction process as performed by the LHCb tracking system, is used to produce high level objects like tracks and vertices. These, in turn, are stored in files formatted identically to the output format of the LHCb event building farm (so called Data Summary Tape). The Brunel application is data-type agnostic: that is, both simulated and collision data are processed in the same way. The simulated DST files can be further processed in an identical manner as real data are.

**Charge generation:** the MCHit objects that are produced by Gauss application and contain such data as sensitive material entry and exit points and energy loss are subsequently used to simulate detector hits. Using the deposited energy value for each particle, the corresponding number of electron-hole pairs are calculated. This generated charge is then distributed along a particle’s path within the silicon.

**Charge deposition:** the deposition process progresses in steps (where the number of steps is a tuneable parameter) and has three components: the constant core ionization, random ionization and high energy  $\delta$ -ray emission. The relative contribution of these three components is tuneable, although the high energy electron production is simulated in ‘a posteriori mode’.

**Delta ray emission:** the energy of emitted  $\delta$ -rays is recovered by comparing the total generated charge and distributed one — if the difference is larger than a given cutoff value, the emission process is simulated at a randomly chosen point on the particle’s path within active material.

**Charge propagation:** finally, the total distributed charge is normalized to the total generated charge for consistency. The distributed charges are then propagated through the sensitive material using a simple, fast projection method: the charge cloud is projected along the estimated particle trajectory direction and no additional secondary interactions are simulated. In case of the VELO the residual magnetic field is ignored, thus, no trajectory tilt is simulated. At each point, a random lateral diffusion is estimated by sampling a Gaussian distribution and then the charges are placed at the surface of the sensor.

**Charge collection:** at the stage of charge collection point, radiation damage effects are taken into account, if necessary, changing appropriately the depletion depth and as a result the collected charge distribution and taking into account the second metal layer effect. The charge distribution is adjusted by decreasing the active depth of the depleted bulk of the sensor using test beam data obtained for sensors irradiated with different fluences and bias voltages. The collected signal (in keV) measured as a function of the bias voltage at test beams was fitted with the model:

$$s_{eV} = A \times \sqrt{V_b + B}, \quad (42)$$

with  $s_{eV}$  the observed signal and  $V_b$  the bias voltage applied to the studied sensor. The charge distribution is adjusted using a lookup table of the charge loss as a function of the track position on the sensor, its distance to the strip implant and the track angle expressed in pseudorapidity.

In this pragmatic approach, a simple linear electric field is assumed, and no transient currents are simulated at the sensor collecting electrodes. Using local information on sensor segmentation topology

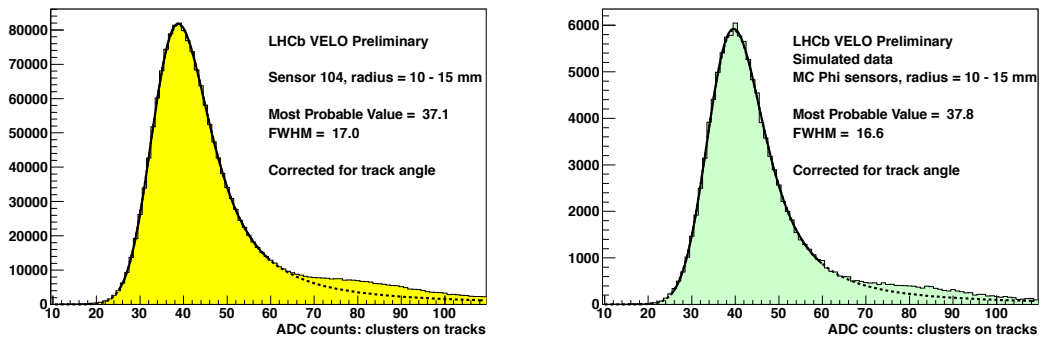


**Fig. 124:** Energy distribution, measured in arbitrary ADC counts, fitted with a model representing Landau convoluted with a Gaussian for a selected VELO sensor. Left hand-side plot is obtained using collision data whilst the right-side hand one presents simulated data. Plots are not normalized.

from a detector model description, a list of channels with collected charges is created.

**Digitization:** the list is next passed to the readout emulation code that adds electronic noise, introduces capacitive couplings between channels, perform digitization and finally applies activation cuts (zero suppression) and performs clusterization (hit reconstruction). The last step is the cluster data encoding into the format that is identical with the transport protocol of respective detectors (also called RawBank) that is the input data for the LHCb Brunel application for track reconstruction. In order to reproduce the clusterization and encoding exactly the emulation and calibration software were partially ported into the simulation platform [54].

**Simulation results:** the results of the simulation process can be broadly divided into two categories: low level, including Landau distribution of deposited energy and its dependency on the local position on a sensor, hit rates, occupancies etc.; and high level, such as track multiplicity, primary and secondary vertices, single hit resolution, vertex resolution, geometrical impact parameter resolution etc.

The latter set of variables need full track reconstruction to be performed. Some of these observables are frequently compared to the corresponding observables obtained from data. Specifically, the primary vertex resolution is monitored by means of lifetime measurements, the impact parameter resolution using selection algorithms, the spatial resolution using track fitting, and Landau distributions are measured using hit reconstruction and their association with tracks and radiation damage studies. Selected results are shown in Figs. 124 and 125, demonstrating well-simulated Landau curves and spatial single hit resolution.

**Summary:** the silicon simulation software is an essential part of the detector performance studies (including radiation damage effects) and physics analyses performed by LHCb collaboration. The quality of the simulated samples is continuously improved and cross-checked against the collision data. The constant maintenance and improvements of the simulation code, often using the feedback from measurements, is crucial.

#### 7.4 Discussion and outlook

Thanks to the excellent luminosity performance of the LHC the effects of radiation damage are visible on silicon tracking sensors of the LHC experiments. The degradation of charge collection efficiency and spatial resolution was sizeable during Run 2, up to the point that it was necessary to modify detector conditions, changing bias voltage, threshold settings, temperature and more. While these measures allowed to keep collecting good data for physics, it was necessary to implement corrections to Monte Carlo simulations to take into account the modified performance of the silicon detectors. As presented in this Section, the LHC experiments implemented methods to correct MC simulations for the radiation

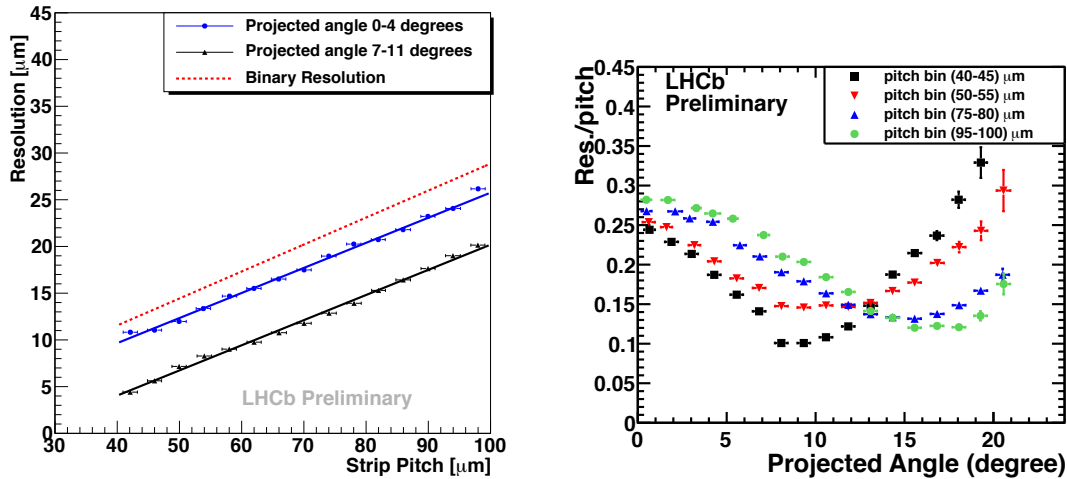


**Fig. 125:** Single hit spatial resolution measured for the LHCb VELO detector. Left: resolution as a function of the sensor pitch for two different track angles and compared to the binary resolution. Right: the resolution as a function of track angle for different pitch regions.

damage to silicon tracking sensors.

**ALICE**, like **ATLAS**, **CMS**, and **LHCb**, uses simulations of their pixel sensors for signal predictions in their sensors. However, radiation effects were not taken into account in these simulations, as their levels of radiation were quite low compared to those of the other three experiments; see also Sections 4 and 3.2.

**LHCb** implemented radiation damage in the step of charge collection by correcting for the depletion depth. The electric field is assumed to be linear. Charge loss is estimated from lookup tables with charge losses for different positions on a sensor, distances from implants and track angles. The lookup tables are based on models fitted to bias voltage scans in test beam data.

**ATLAS** calculates signal loss per pixel cell at the digitization step, that is, right after charge deposition by **Geant4**. This method relies on pre-calculated lookup tables for the needed quantities such as electric field, Lorentz angle, trapping rates, and Ramo potential; some of these are obtained using **TCAD** software. Such a strategy allows the calculation of radiation damage effects to be fast enough to be indeed included directly in the Monte Carlo simulation.

**CMS**, following a different approach with respect to **ATLAS**, applies *a posteriori* corrections to the Monte Carlo simulated events. The corrections are based on templates built from data using **PixelAV** and accurate silicon device simulations, the latter obtained using **TCAD** tools. The corrections are applied at cluster level, correcting for the signal amplitude and cluster shape. Trapping constants and donor and acceptor concentration parameters used in the **TCAD** and **PixelAV** software are derived from data.

Whereas in **ATLAS** parameters such as trapping parameters, electron and hole cross-sections in donor and acceptors, and existing models are used for parameters such as trapping rates and defects, **CMS** adjusts these parameters according to measurements from data around twelve times a year.

**Outlook** **TCAD** is widely used to compute the electric field for input to sensor simulation. This program, however, is proprietary, and computationally intensive. Simulations of charge transport could benefit from a viable open source alternative to **TCAD**. There are open source alternatives for technology computer aided design, but not with all capabilities that for example **Silvaco** or **Synopsys** have to offer. While for **CMS** the fitting of parameters to data seems to work quite well, it is not guaranteed that extrapolating such fitted parameters to future fluences would give a good prediction of a future detector's performance. **CMS** created new fits to data multiple times a year to accurately simulate charge transport

in the irradiated detector. Extrapolations to future datasets were made for making future predictions, but not for tracking and simulation for past datasets. Comparisons to data from LHC experiments is important, as irradiation of test beam devices that are often irradiated under controlled conditions can yield performance results deviating by large from radiation damage from LHC collisions. For example, PixelAV found that parameters derived from test beam data did not give an accurate description of the data taken during LHC operation. A model of radiation damage accurately modelling sensor responses as seen in LHC data would give more confidence in such a model being correct for future predictions. The community could benefit from such a description of radiation damage that would fit the data of all four LHC experiments. In addition, it would be beneficial to implement such a model in a framework that can be used to produce simulations of performance measurements so that it can be compared to both test beam and detector data.

## References

- [1] W. Shockley, *J. Appl. Phys.* **9** (1938) 635, doi:10.1063/1.1710367.
- [2] S. Ramo. *Proc. IRE* **27** (1939) 584, doi:10.1109/JRPROC.1939.228757.
- [3] M. Aaboud *et al.* [ATLAS Collaboration], *JINST* **14** (2019) P06012, doi:10.1088/1748-0221/14/06/P06012.
- [4] J. Idarraga and M Benoit, [The A11Pix simulation framework](#), last accessed July 12, 2020.
- [5] G. Kramberger, [KDetSim](#) – a simple way to simulate detectors, last accessed July 16th, 2020.
- [6] M. Swartz, [A detailed simulation of the CMS Pixel Sensor](#), CMS NOTE-2002/027, (CERN, Geneva, 2002).
- [7] V. Chiochia *et al.*, *IEEE Trans. Nucl. Sci.* **52** (2005) 1067, doi:10.1109/TNS.2005.852748, arXiv:physics/0411143.
- [8] M. Swartz *et al.*, *Nucl. Instrum. Meth.* **A565** (2006) 212, doi:10.1016/j.nima.2006.05.002, arXiv:physics/0510040.
- [9] S. Spannagel *et al.* *Nucl. Instrum. Meth.* **A901** (2018) 164, doi:10.1016/j.nima.2018.06.020
- [10] ATLAS Collaboration, *JINST* bf 3 (2008) S08003, doi:10.1088/1748-0221/3/08/S08003.
- [11] G. Aad *et al.* *JINST* **3** (2008) P07007, doi:10.1088/1748-0221/3/07/P07007.
- [12] [ATLAS inner detector: Technical design report, Vol. 1](#), ATLAS Collaboration, ATLAS-TDR-4, CERN-LHCC-97-16, (CERN, Geneva, 1997).
- [13] [ATLAS inner detector: Technical design report, Vol. 2](#), ATLAS Collaboration, ATLAS-TDR-5, CERN-LHCC-97-17, (CERN, Geneva, 1997).
- [14] ATLAS Collaboration, [ATLAS Insertable B-Layer technical design report](#), ATLAS-TDR-19, CERN-LHCC-2010-013 (CERN, Geneva, 2010).
- [15] ATLAS Collaboration, *JINST* **13** (2018) T05008, 10.1088/1748-0221/13/05/T05008.
- [16] ATLAS Collaboration, [Radiation damage in 2015-2017](#), PIX-2018-005, 2018.
- [17] S. Agostinelli *et al.*, *Nucl. Instrum. Meth.* **A506** (2003) 250, doi:10.1016/S0168-9002(03)01368-8, CERN-IT-2002-003.
- [18] ATLAS Offline Software, [ATLAS Athena Guide](#), last accessed July 12, 2020.
- [19] T. Sjöstrand *et al.*, *Comput. Phys. Commun.* **191** (2015) 159, doi:10.1016/j.cpc.2015.01.024, arXiv:1410.3012 [hep-ph].
- [20] A. Ferrari *et al.*, FLUKA: A multi-particle transport code (program version 2005), CERN Yellow Reports: Monographs, CERN-2005-010 (CERN, Geneva, 2005), doi:10.5170/CERN-2005-010.
- [21] ATLAS Collaboration, [Measurements and predictions of Pixel Detector leakage current](#), 2018.
- [22] V. Chiochia *et al.* *Nucl. Instrum. Meth.* **A568** (2006) 51, doi:10.1016/j.nima.2006.05.199, arXiv:physics/0506228.

- [23] F. Moscatelli *et al.*, *IEEE Trans. Nucl. Sci.* **63** (2016) 2716, [10.1109/TNS.2016.2599560](https://doi.org/10.1109/TNS.2016.2599560), [arXiv:1611.10138](https://arxiv.org/abs/1611.10138) [physics.ins-det].
- [24] ATLAS Collaboration, [ATLAS PIX-2018-004](#).
- [25] A. Zeng Wang and B. N. Philip Nachman [ATLAS Collaboration], [dE/dx simulation plots for Run 2](#), PIX-2018-004, 2018.
- [26] V Wallangen [ATLAS Collaboration], *PoS Vertex 2017* (2018) 050, [doi:10.22323/1.309.0050](https://doi.org/10.22323/1.309.0050).
- [27] G.F. Dalla Betta, *PoS IFD2014* (2015) 013, [doi:10.22323/1.219.0013](https://doi.org/10.22323/1.219.0013).
- [28] C. Da Via *et al.*, *Nucl. Instrum. Meth.* **A699** (2013) 18, [doi:10.1016/j.nima.2012.05.070](https://doi.org/10.1016/j.nima.2012.05.070).
- [29] O. Krasel *et al.*, *IEEE Trans. Nucl. Sci.* **51** (2004) 3055, [doi:10.1109/TNS.2004.839096](https://doi.org/10.1109/TNS.2004.839096).
- [30] G. Kramberger *et al.*, *Nucl. Instrum. Meth.* **A481** (2002) 297, [doi:10.1016/S0168-9002\(01\)01263-3](https://doi.org/10.1016/S0168-9002(01)01263-3), ATL-INDET-2002-006.
- [31] G. Alimonti *et al.*, [A study of charge trapping in irradiated silicon with test beam data](#), ATL-INDET-2003-014 (CERN, Geneva, 2003).
- [32] ATLAS Collaboration, [Charge Collection Efficiency as a function of integrated luminosity](#), 2017.
- [33] Synopsis Inc., [TCAD](#), last accessed July 12, 2020.
- [34] ATLAS Collaboration, [Radiation damage to the ATLAS pixel and Lorentz angle](#), PIX-2017-005, 2017.
- [35] D.M. Caughey and R.E. Thomas, *Proc. IEEE* **55** (1967) 2192, [doi:10.1109/PROC.1967.6123](https://doi.org/10.1109/PROC.1967.6123).
- [36] C. Canali *et al.*, *IEEE Trans. Electron Devices* **22** (1975) 1045, [doi:10.1109/T-ED.1975.18267](https://doi.org/10.1109/T-ED.1975.18267).
- [37] ATLAS Collaboration, [Modeling the mobility and Lorentz angle for the ATLAS Pixel Detector](#), ATL-INDET-PUB-2018-001 (CERN, Geneva, 2018).
- [38] C. Jacoboni *et al.*, A review of some charge transport properties of silicon, *Solid State Electron.* **20** (1977) 77, [doi:10.1016/0038-1101\(77\)90054-5](https://doi.org/10.1016/0038-1101(77)90054-5).
- [39] J. Becker *et al.*, *Solid State Electron.* **56** (2011) 104, [doi:10.1016/j.sse.2010.10.009](https://doi.org/10.1016/j.sse.2010.10.009), [arXiv:1007.4432](https://arxiv.org/abs/1007.4432) [physics.ins-det].
- [40] CMS Offline Software, [CMSSW](#), last accessed July 12, 2020.
- [41] H. Bichsel, *Nucl. Instrum. Meth.* **A562** (2006) 154, [doi:10.1016/j.nima.2006.03.009](https://doi.org/10.1016/j.nima.2006.03.009); H. Bichsel, *Rev. Mod. Phys.* **60** (1988) 663, [doi:10.1103/RevModPhys.60.663](https://doi.org/10.1103/RevModPhys.60.663).
- [42] M. Swartz *et al.*, *PoS Vertex 2007* 035, [doi:10.22323/1.057.0035](https://doi.org/10.22323/1.057.0035).
- [43] S. Cucciarelli, D. Kotlinski, T. Todorov, [Position Determination of Pixel Hits](#), CMS-NOTE-2002-049, (CERN, Geneva, 2002).
- [44] G. Giurgiu *et al.* [CMS Collaboration], [arXiv:0808.3804](https://arxiv.org/abs/0808.3804) [physics.ins-det].
- [45] Pixel Charge Profiles, [Performance plots for Phase 1 Pixel Detector, August 2018](#). Last accessed October 12, 2020.
- [46] Pixel Charge Profiles in Run-2 Data and Simulation, CMS Collaboration, May 2020, [CMS-DP-2020-026](#).
- [47] R. Ranieri, The simulation of the CMS Silicon Tracker, 2007 IEEE Nuclear Science Symposium Conference Record, Honolulu, HI, 2007, pp. 2434-2438, [doi:10.1109/NSSMIC.2007.4436649](https://doi.org/10.1109/NSSMIC.2007.4436649), [CMS-CR-2008-007](#).
- [48] Evolution of S/N during Run II, [CMS Silicon Strip Performance Results 2018](#). Last accessed October 12, 2020.
- [49] Silicon Strip Tracker Performance results 2018, CMS Collaboration, September 2018, [CMS-DP-2018-052](#).
- [50] LHCb Collaboration, [The Gauss project](#), last accessed July 12, 2020.
- [51] J. Allison *et al.*, *Nucl. Instrum. Meth.* **A835** (2016) 186, [doi:10.1016/j.nima.2016.06.125](https://doi.org/10.1016/j.nima.2016.06.125).
- [52] LHCb Collaboration, [The Boole project](#), last accessed July 12, 2020.

[53] LHCb Collaboration, [The Brunel project](#), last accessed July 12, 2020.

[54] L. Bel *et al.*, *J. Phys. Conf. Ser.* **898** (2017) 092046, [doi:10.1088/1742-6596/898/9/092046](https://doi.org/10.1088/1742-6596/898/9/092046).